Metastability in a nanobridge-based hysteretic dc SQUID embedded in a superconducting microwave resonator

Eran Segev,[*] Oren Suchoi, Oleg Shtempluck, Fei Xue,[†] and Eyal Buks
Department of Electrical Engineering, Technion, Haifa IL-32000, Israel
(Received 29 July 2010; revised manuscript received 20 November 2010; published 17 March 2011)

We study the metastable response of a highly hysteretic dc superconducting quantum interference device (SQUID) made of a niobium loop interrupted by two nanobridges. We excite the SQUID with an alternating current and with direct magnetic flux, and find different stability zones forming diamond-like structures in the measured voltage across the SQUID. When such a SQUID is embedded in a transmission line resonator, similar diamond structures are observed in the reflection pattern of the resonator. We calculate the dc-SQUID stability diagram in the plane of the exciting control parameters, both analytically and numerically. In addition, we obtain numerical simulations of the SQUID equations of motion, taking into account temperature variations and nonsinusoidal current-phase relation of the nanobridges. Good agreement is found between experimental and theoretical results.

DOI: 10.1103/PhysRevB.83.104507 PACS number(s): 85.25.Dq, 74.40.Gh, 74.25.Sv

I. INTRODUCTION

In the last two decades, superconducting quantum interference devices (SQUIDs) have regained the interest of researchers worldwide due to the use of SQUIDs as solid-state quantum bits. More recently, such SQUIDs were embedded in superconducting transmission line resonators (TLRs) in order to produce circuit cavity quantum electrodynamics in the strong[1–6] and the dispersive[7–9] coupling regimes.[10] Other applications, in which SQUIDs are mainly used as nonlinear classical elements, include Josephson bifurcation amplifiers[11–14] and tunable resonators.[15–17] Tunable resonators were also used to demonstrate parametric amplification and squeezing[18–21] and might also be used to demonstrate the dynamical Casimir effect.[22,23]

The injected power into a TLR is usually limited by the critical current of the dc SQUID embedded in the resonator. The upper bound of this current is determined by the sum of the two critical currents of the Josephson junctions (JJs) composing the dc SQUID. While typical critical currents of dc SQUIDs range between a few to a tenth of microamperes, the applications that involve resonance tuning and parametric amplification could benefit from larger critical currents. To have larger critical currents, one can fabricate dc SQUIDs using nanobridges instead of JJs. Nanobridges, which are merely artificial weak links having submicron size, were shown to have similar current-phase relationship (CPR) as JJs under certain conditions.[24–26] These nanobridge JJs (NBJJs) are characterized by large critical current, on the order of milliamperes.[27,28] The dc SQUIDs with large critical currents are often characterized by hysteretic response and metastable dynamics.[29–33] These characters are naturally made extreme in NBJJ-based dc SQUIDs. In addition, NBJJs have very high plasma frequency,[34] on the order of one terahertz, which enables operation of the microwave TLR without introducing interstate transitions in the embedded SQUID. Thus, one could employ a SQUID as a nonlinear lumped inductor, operating at microwave frequencies.

In this paper, we experimentally and numerically study metastable response of NBJJ-based dc SQUID, subjected to an alternating biasing current. We first theoretically analyze stability zones of a highly hysteretic dc SQUID in the plane of the bias current and magnetic flux control parameters. Then we directly measure the voltage across a dc SQUID in that plane. Comparison between experimental results and between analytical and numerical theoretical predictions yield good agreement. Moreover, we measure the reflection spectra from several devices integrating a SQUID and a TLR and find qualitative agreement between the theory and the experiments.

II. EXPERIMENTAL SETUP

A simplified circuit layout of our devices is illustrated in the enclosed dashed rectangular area in Fig. 1. We fabricate our devices on high resistivity silicon wafers, each covered by a thin layer of silicon nitride. Each device is made of niobium, having layer thickness of less than 100 nm, and is composed of a stripline resonator having a dc SQUID embedded in its structure. The resonator is designed to operate in the gigahertz range, having a length of $l = 19$ mm, which sets its first resonance mode at about 2.5 GHz. The dc-SQUID spatial location relative to the resonator boundaries is optimized for achieving the best coupling between the SQUID and the second resonance mode of the resonator, i.e., a resonance mode at about 5GHz. The dc SQUID is composed of two NBJJs, one NBJJ in each of its two arms [see Fig. 2(b) and inset of Fig. 3]. The NBJJs are fabricated using FEI Strata 400 focused ion beam system[27,35] at an accelerating voltage of 30 kV and gallium ions current of 1.5 pA. The outer dimensions of the bridges range from 100×100 nm^2 for large junctions to 60×80 nm^2 for relatively small ones. The actual dimensions of the weak links are smaller because the bombarding gallium ions penetrate into the niobium layer, and consequently suppress superconductivity over a depth estimated between 30 to 50 nm.[27,36,37] Despite the small dimensions of our NBJJs, most of our SQUIDs have critical currents on the order of milliamperes (see Table I). A feedline, weakly coupled to the resonator, is employed for delivering input and output signals. An on-chip transmission line passes near the dc SQUID and is used to apply magnetic flux through the dc SQUID at frequencies ranging from dc to the gigahertz.

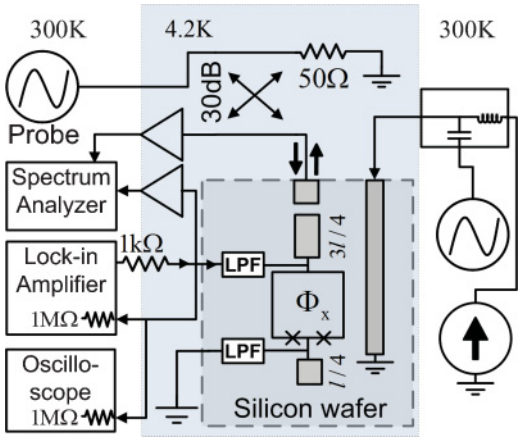

FIG. 1. (Color online) Measurement and experimental setup. The enclosed dashed rectangular area shows an unscaled schematic layout of our device.

An on-chip filtered dc bias line is connected directly to the dc SQUID and is used for direct measurements of the SQUID. The low-pass filters (LPFs) are designed to minimize the degrading effect of these connections on the quality factor of the resonator. Some measurements are carried out while the device is fully immersed in liquid helium, while others are carried out in a dilution refrigerator where the device is in vacuum. Further design considerations and fabrication details can be found elsewhere.[34,38]

The experimental results in this paper are obtained from three devices, the parameters of which are summarized in Table I. The experiments are carried out using the setup depicted in Fig. 1. We report on two types of experiments. In the first one, we obtain low-frequency current-voltage measurements of the SQUID using the dc bias line, while the resonator does not play any role. We use a lock-in amplifier, which applies alternating current through the SQUID, having excitation frequencies on the order of kilohertz. We measure the voltage across the SQUID using the lock-in amplifier and, in addition, we record the spectral density of the voltage using a spectrum analyzer and its time-domain dynamics using an oscilloscope. In the second type of experiment, we investigate the response of an integrated SQUID-TLR device to a monochromatic incident probe tone that drives one of the

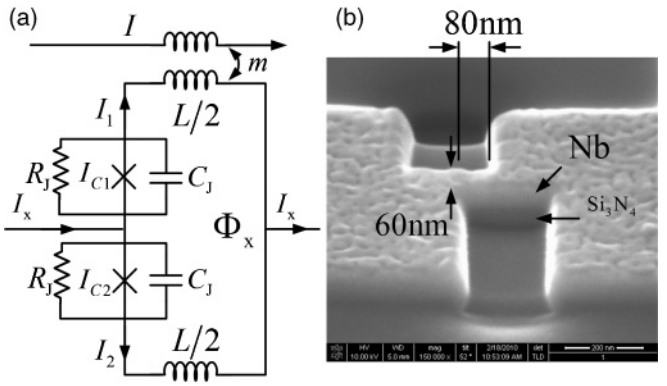

FIG. 2. (a) Circuit model of a dc SQUID. (b) Electron micrograph of a nanobridge, the dimensions of which are $80 \times 60 \times 50$ nm^3.

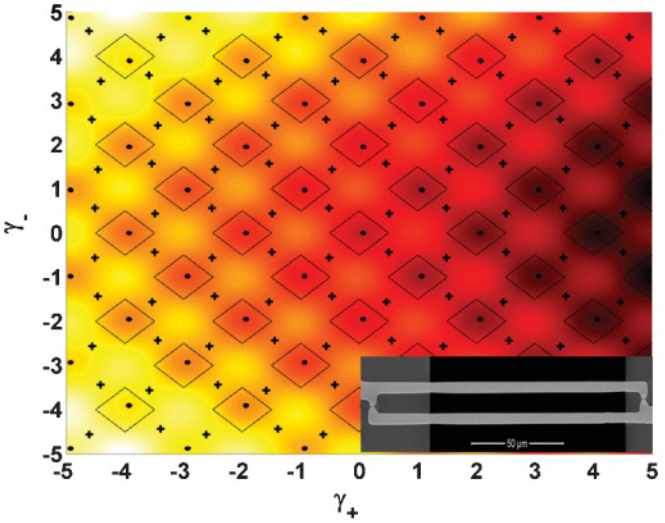

FIG. 3. (Color online) Potential diagram of a dc SQUID $u(\gamma_+,\gamma_-)$, drawn using $I_x = 0.1I_c$ and $\Phi_x = 0$. Local minima points are labeled by black dots and saddle points are labeled by plus signs. The inset shows an electron micrograph of a dc SQUID.

resonance modes of the TLR. The reflected power spectrum is recorded by a spectrum analyzer. In such experiments, the dc bias line is left floating and, thus, does not play any role in the measurement. In both types of experiments, we apply dc magnetic flux through the SQUID, and in experiments with TLRs, we also add modulated magnetic flux at gigahertz frequencies.

A. Numerical method

Simulations of the dc SQUID circuit model [see Fig. 2(a)] are done by numerically integrating its equations of motion (EOMs) [Eqs. (7) and (8)]. We introduce a sinusoidal excitation current to the EOMs and calculate the phases of the two NBJJs composing the dc SQUID, the dc-SQUID voltage versus time, and the Fourier transform of this voltage at the frequency of excitation.

The excitation frequencies in the low-frequency current-voltage experiments were usually around 1 kHz. This frequency range is about nine orders of magnitude smaller

TABLE I. SQUID parameters. The self-inductance was numerically calculated using FASTHENRY computer program (Ref. 39). The parameter β_L Calc was evaluated analytically using the measured critical current. The parameters β_L Fit, $\widetilde{\beta_L}$ Fit, and α Fit were evaluated according to fittings of stability diagrams to measured data.

Parameter	$E19$	$E38$	$E42$
SQUID type	rf	dc	dc
SQUID area (μm^2)	1936	870	1057
Nb thickness (nm)	50	100	60
Self-inductance (pH)	127	112	141
I_c(mA)		3.24	2.46
β_L Calc		1089	106
β_L Fit		722	83
$\widetilde{\beta_L}$ Fit	1.5		45,35
α Fit		0.026	0.032

than the SQUID plasma frequency and about six orders of magnitude smaller than the rate of thermal processes in the NBJJs.[40] Therefore, in order to make simulations of such experiments feasible in terms of computation time, we have to make two simplifying assumptions. We first assume that the excitation frequency used in simulation can be made much higher than the one used in the experiments. This assumption holds as long as the dynamics of the dc SQUID follows the excitation current adiabatically. Adiabatic approximation of NBJJs based DC-SQUID is thoroughly analyzed in Ref. 34, where it is shown that the plasma frequency of NBJJs-based dc SQUID is expected to be on the order of 1THz. Thus, in practice, the excitation frequencies used in simulation are set between 100MHz and 1GHz. We further assume that thermal processes had a negligible influence on the measured dynamics of the SQUID during the low-frequency current-voltage experiments. This assumption holds because the devices used to obtain the experimental data in this paper have not shown any hysteretic behavior during those measurements.[41] Thus, the temperature of the SQUID is held at base temperature throughout the simulation and does not evolve with the SQUID dynamics. Only in simulations related to measurements done with an integrated TLR-SQUID device, in which the measurement frequency is high, are thermal effects taken into account by including thermal EOMs [Eq. (16)].

III. THEORY OF HYSTERETIC dc SQUID

In this section, we develop a theory of hysteretic and metastable dc SQUID, taking into account the self-inductance and asymmetry of the dc SQUID. Similar models were also developed by others, but usually lacking comparison with experimental data[10,29,32,42–45] or emphasizing other aspects of SQUID dynamics.[31,46,47] We begin with a lossless model in order to extract the SQUID stability diagram, and add the dissipation and fluctuation terms to the EOMs at a later stage.

The circuit model is shown in Fig. 2(a) (an electron micrograph can be seen in the inset of Fig. 3). It contains a dc SQUID having two NBJJs, one in each of its arms. The NBJJs have critical currents of I_{c1} and I_{c2}, which, in general, may differ one from another. Both NBJJs are assumed to have the same shunt resistance R_J and capacitance C_J [which is considered extremely small for NBJJs (Ref. 48)]. The self-inductance L of the dc SQUID is assumed to be equally divided between its two arms. Typical inductance values of our SQUIDs are listed in Table I.

The dc SQUID is controlled by two external parameters. The first is bias current $I_x = I_1 + I_2$, where I_1 and I_2 are the currents flowing in the upper and lower arms of the dc SQUID, respectively [Fig. 2(a)]. The second is external magnetic flux Φ_x applied through the dc SQUID. The total magnetic flux threading the dc-SQUID loop is given by $\Phi = \Phi_x + LI_-$, where $I_- = (I_1 - I_2)/2$ is the circulating current in the loop. Assuming sinusoidal CPR, the Josephson current I_{Jk} in each junction ($k = 1,2$) is related to the critical current I_{ck} and to the Josephson phase γ_k by the Josephson equation $I_{Jk} = I_{ck}\sin\gamma_k$. By employing the coordinate transformation $\gamma_+ = (\gamma_1 + \gamma_2)/2$ and $\gamma_- = (\gamma_1 - \gamma_2)/2$, and the notation $I_c = (I_{c1} + I_{c2})$ and $I_{c-} = (I_{c1} - I_{c2})$, one finds that the potential governing the dynamics of the dc SQUID is given by[31]

$$\frac{u}{E_0} = -\cos\gamma_+\cos\gamma_- + \alpha\sin\gamma_+\sin\gamma_- + \left(\gamma_- + \frac{\pi\Phi_x}{\Phi_0}\right)^2 \Big/ \beta_{\mathrm{L}} - \frac{I_x}{I_c}\gamma_+ , \tag{1}$$

where $\beta_L = \pi L I_c/\Phi_0$ is a dimensionless parameter characterizing the dc SQUID hysteresis, $\alpha = I_{c-}/I_c$ characterizes the dc SQUID asymmetry, $E_0 = (\Phi_0 I_c)/2\pi$ is the Josephson energy, and Φ_0 is the flux quantum.

A. Stability zones

The extrema points of the dc SQUID potential are found by solving

$$\frac{\partial u}{\partial\gamma_+} = \sin\gamma_+\cos\gamma_- + \alpha\cos\gamma_+\sin\gamma_- - \frac{I_x}{I_c} = 0, \tag{2}$$

$$\frac{\partial u}{\partial\gamma_-} = \cos\gamma_+\sin\gamma_- + \alpha\sin\gamma_+\cos\gamma_- + \frac{2\gamma_-}{\beta_L} + \frac{2\pi\Phi_x}{\Phi_0\beta_L} = 0. \tag{3}$$

In general, Eqs. (2) and (3) have periodic solutions, where the solutions differ one from another by $2\pi m_+$ in γ_+, $2\pi m_-$ in γ_-, and by $2\Phi_0 m_-$ in Φ_x, where m_+ and m_- are integers.

The Hessian of the potential u is given by

$$H = \begin{pmatrix} \frac{\partial^2 u}{\partial\gamma_+^2} & \frac{\partial^2 u}{\partial\gamma_+\partial\gamma_-} \\ \frac{\partial^2 u}{\partial\gamma_-\partial\gamma_+} & \frac{\partial^2 u}{\partial\gamma_-^2} \end{pmatrix}. \tag{4}$$

For local minima points of the potential, both eigenvalues of H are positive. Thus, we find boundaries of stability regions of these minima points in the plane of the JJ phases γ_+ and γ_- by demanding that

$$\det H = 0, \qquad \mathrm{tr}H > 0. \tag{5}$$

Furthermore, the matrix H is independent on both control parameters I_x and Φ_x; thus, these boundaries are also independent on I_x and Φ_x. Finding the stability thresholds in the plane of I_x and Φ_x is done by substituting the solutions of Eq. (5) in Eqs. (2) and (3).

Figure 3 plots the potential diagram of a dc SQUID, calculated for $E42$ using $\beta_L = 83$ and $\alpha = 0.032$. The solution of Eq. (5) produces the black closed curves that enclose the dc SQUID local minima points in the plane of γ_+ and γ_-. The local minima points are labeled by black dots and saddle points are labeled by plus signs. A local minimum point loses its stability when increasing either $|I_x|$ or $|\Phi_x|$ to a point where it merges with one of the saddle points close to it.

1. *The limits of small and large β_L*

In general, solving Eqs. (2) and (3) for a given set of γ_+ and γ_- can only be done numerically. An analytical solution can

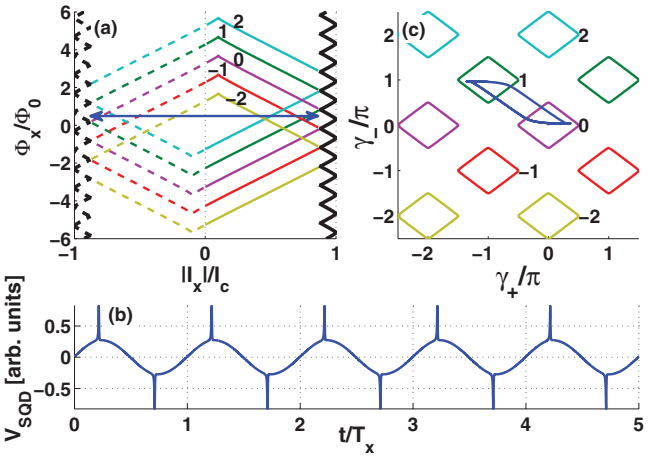

FIG. 4. (Color online) (a) Stability diagram in the plane of the control parameters I_x and Φ_x, drawn for $\beta_L = 20$ and $\alpha = 0.1$. The curves are plotted using solid line for $I_x > 0$ and dashed line for $I_x < 0$. The number close to each curve labels the number of flux quanta trapped in the dc SQUID in the corresponding LSZ. Corresponding numbers are also indicated in panel (c). The bold black curve marks the threshold between static and oscillatory zones. The double-headed arrow is drawn between the points $I_x = \pm 0.9 I_c$, $\Phi_x = 0.52\Phi_0$, and marks the control parameter range used in the numerical simulation shown in panels (b) and (c). These panels show SQUID voltage in the time domain (b) and the NBJJs phases in the phase space (c). The time scale is normalized by the period of excitation $T_x = \omega_x/2\pi$.

be derived only for the extreme limits of $\beta_L \ll 1$ and $\beta_L \gg 1$. In the former limit, which is not the focus of this paper, the derivation leads to the well-known formula for the SQUID critical current[49]

$$\sqrt{1-(1-\alpha^2)\sin^2\frac{\pi\Phi_x}{\Phi_0}} = \frac{I_x}{I_c}. \tag{6}$$

In the opposite limit of $\beta_L \gg 1$, the condition of $\det H = 0$ implies that $\cos\gamma_1 \cos\gamma_2 = 0$, and the condition of $\mathrm{tr}H > 0$ implies that $(1+\alpha)\cos\gamma_1 + (1-\alpha)\cos\gamma_2 > 0$. Consider first the solution for the minimum point near $(\gamma_+,\gamma_-) = (0,0)$. Other solutions can be obtained from the periodic properties of Eqs. (2) and (3). For this solution, Eq. (5) is satisfied along a square that is formed by the lines connecting the four vertices $\gamma_1 = \pm\pi/2$ and $\gamma_2 = \pm\pi/2$. Substituting these vertices into Eqs. (2) and (3) yields a bounding contour, which has a rectangle shape with vertices at $(I_x/I_c, 2\pi\Phi_x/\Phi_0\beta_L) = (1,\alpha)$, $(\alpha,1)$, $(-1,-\alpha)$, and $(-\alpha,-1)$ in the plane of the control parameters I_x and Φ_x [see Fig. 4(a)]. This rectangle crosses the vertical axis ($I_x = 0$) at the points $\Phi_x = \pm\Phi_0(1-\alpha)\beta_L/2\pi$ and the horizontal axis ($\Phi_x = 0$) at the points $I_x = \pm I_c(1-\alpha)$.

B. Equations of motion

Applying Kirchhoff's laws to the dc SQUID circuit model, substituting Josephson's current-phase and voltage-phase equations, and taking into account the fluctuation dissipation theory, yield the following EOMs for the SQUID phases γ_1 and γ_2 (Ref. 49):

$$\ddot{\gamma}_1 + \beta_D\dot{\gamma}_1 + (1+\alpha_0)y(\Theta_1)\sin\gamma_1 + \frac{1}{\beta_{L0}}(\gamma_1 - \gamma_2 + 2\pi\Phi_x/\Phi_0) = I_x/I_{c0} + g_{n1}, \tag{7}$$

$$\ddot{\gamma}_2 + \beta_D\dot{\gamma}_2 + (1-\alpha_0)y(\Theta_2)\sin\gamma_2 - \frac{1}{\beta_{L0}}(\gamma_1 - \gamma_2 + 2\pi\Phi_x/\Phi_0) = I_x/I_{c0} + g_{n2}, \tag{8}$$

where the overdot denotes derivative with respect to a normalized time parameter $\tau = \omega_{\mathrm{pl}}t$, where ω_{pl} is the SQUID plasma frequency, and $\beta_D = 1/(R_J C_J \omega_{\mathrm{pl}})$ is the damping coefficient. In general, the NBJJ critical current I_{ck} ($k = 1,2$), and thus I_c and I_{c-}, are temperature dependent, as we discuss later. Thus, we employ the notation I_{c0k}, I_{c0}, and I_{c0-} for the corresponding critical currents at a base temperature T_0, which is the temperature of the coolant. In addition, we employ the notation $\beta_{L0} = \pi L I_{c0}/\Phi_0$ and $\alpha_0 = (I_{c01} + I_{c02})/(I_{c01} - I_{c02})$. The term $y(\Theta_k)$, where $\Theta_k = T_k/T_c$ is the normalized temperature of the kth NBJJ, expresses the dependence of the NBJJ critical current on its temperature, and is equal to unity as long as the temperature of the NBJJ is held at base temperature. The factor g_{nk} is a noise term, with the spectral density for the case where $h\nu/k_{\mathrm{B}}T \ll 1$ given by $S_{I_n}(\nu) = 4k_{\mathrm{B}}T/R_J$, with k_{B} being the Boltzmann constant. In what follows, we neglect this noise term in the numerical simulations.

To evaluate the voltage across the dc SQUID, which is denoted as V_{SQD}, we assume that the loop inductance is equally divided between its two arms, and get

$$V_{\mathrm{SQD}} = \frac{1}{2}\left[\frac{\Phi_0}{2\pi}\left(\frac{d}{\gamma_1}dt + \frac{d\gamma_2}{dt}\right) + \frac{L}{2}\frac{dI_x}{dt}\right]. \tag{9}$$

It is known that NBJJs may have complex CPR,[25,50,51] which deviates from the normal sinusoidal CPR of a regular JJ. According to a theory presented in the Appendix for completeness, such deviation would modify the $\sin\gamma_i$ term in the SQUID EOMs [Eqs. (7) and (8)], which become Eqs. (A5) and (A6). We have made some simulations in which moderate changes in the CPR of our SQUIDs are assumed, and found no significant difference between these results and results that neglect this deviation. In addition, the physical dimensions of our NBJJs are relatively small, and the measured values of β_L of our SQUIDs are relatively high, thus following the explanations detailed in Appendix A1 of Ref. 34, the effect of nonsinusoidal CPR in our NBJJs is expected to be negligibly small. Therefore, our conclusion is that our SQUIDs can be modeled by normal sinusoidal CPR.

C. Stability diagram

The stability diagrams in the plane of the control parameters I_x and Φ_x, and in the plane of the dc SQUID phases γ_+ and γ_-, are plotted in Figs. 4(a) and 4(c), respectively. The curves were first calculated in the plane of γ_+ and γ_- by numerically solving Eq. (5), with the parameters $\beta_L = 20$ and $\alpha = 0.1$.

The above solutions were then substituted into Eqs. (2) and (3) to produce the closed contours of panel (a). Each closed contour bounds a local stability zone (LSZ) corresponding to a different integer number of flux quanta trapped in the dc SQUID. Corresponding LSZs in Figs. 4(a) and 4(c) are labeled by the same number, indicating the number of trapped flux quanta.

The stability diagram can be separated into two global zones. The first is called the static zone,[46,47] where the system has one or more LSZs depending of the value of the screening parameter β_L. The static zone is bounded in the horizontal axis by a threshold current called the oscillatory threshold, given by $I_{\rm th}(\Phi_x) = I_c - I_-(\Phi_x)$. This threshold is periodic in the external flux Φ_x, having a maximum value equal to the critical current of the dc SQUID. When the dc SQUID is biased to the static zone, it is always found in a LSZ, although transitions between LSZs may be forced by the control parameters. The second zone, called the oscillatory zone[46,47] (also known as the dissipative or free-running zone), spreads over two unbounded regions for which the excitation current is larger (in absolute value) than the oscillatory threshold. In this zone, the dc SQUID has no stable state, and therefore it oscillates at very high frequencies and dissipates energy. In what follows, we focus our study on the static zone. Further study of the dynamics in the region of spontaneous oscillations can be found in Ref. 47.

IV. dc-SQUID LOW-FREQUENCY DYNAMICS

The EOMs, Eqs. (7) and (8), were numerically integrated using the parameters that were used to draw the stability diagram of Fig. 4, and using the control parameters $\Phi_x = 0.52\Phi_0$ and $I_x/I_c = 0.9$. The range of the excitation is marked by a double-headed arrow in the stability diagram of Fig. 4(a). Note that the left arrow head crosses the threshold separating LSZ-0 and LSZ-1 (LSZs corresponding to 0 or 1 trapped flux quanta, respectively), whereas the right-headed arrow crosses the threshold separating LSZ-1 back into LSZ-0. The results of a simulation in which a dc SQUID is periodically excited along this path are shown in Fig. 4(b), which shows the dc-SQUID voltage in the time domain. Each excitation cycle contains two spikes, which occur close to extrema points of the excitation amplitude. Panel (c) shows the simulation in the phase plane of γ_+ and γ_-. The simulation shows that the system periodically switches between LSZ-0 and LSZ-1, and that the dynamics does not involve any additional LSZs. Thus, a positive spike in the time-domain response corresponds to a transition from LSZ-0 to LSZ-1, and a negative spike corresponds to an opposite transition. While the excitation is monotonically increased, the system mostly lingers in LSZ-0, and while it is decreased, it mostly lingers in LSZ-1. Note that the experimental measured voltage, shown for example in Fig. 8, includes a parasitic voltage offset originated by serial parasitic resistance of the wiring in our experimental setup. Thus, in order to qualitatively compare between the experimental and the numerical results, and in order to emphasize the excitation cycle, a parasitic voltage of $V_{\rm paras} = I_x R_{\rm paras}$, where $R_{\rm paras} = 0.5\Omega$, is added to the numerical results. Note also that the duration of each spike, which is related to the relaxation time of the SQUID, is negligible compared to the period of excitation $T_x = 2\pi/\omega_x$. Thus, the assumption that the response of the dc SQUID to the excitation is adiabatic is reasonable.

A. Periodic dissipative static zone

Figure 5 shows a qualitative comparison between experimental results measured with $E38$ using lock-in amplifier [panel (a)] and simulation results calculated using the corresponding parameters [panel (b)]. Both panels show color maps of the voltage across the dc SQUID as a function of control parameters I_x and Φ_x. The black contours in both graphs mark the corresponding stability diagram. The negative part of the stability contours is folded onto the positive part and is drawn by dashed lines. Thus, solid lines represent stability thresholds for positive excitation currents, and dashed lines represent stability thresholds for negative excitation currents. The bold black contour is the threshold between the static and the oscillatory zones.

The folding of the stability contours divides the static zone of the stability diagram into regions having diamond shapes in the plane of I_x and Φ_x. Each diamond-shaped region bounds a range of parameters for which the system crosses the same number of stability thresholds during an excitation cycle. For example, when the dc SQUID is excited with parameters bounded by the diamond region marked by the number 2, it crosses a single threshold during the positive duration of the excitation cycle and another one during the negative duration. The crossing of the threshold back and forth brings back the SQUID to the original LSZ, similar to the case discussed in Fig. 4(c). Each crossing of a threshold line, either by

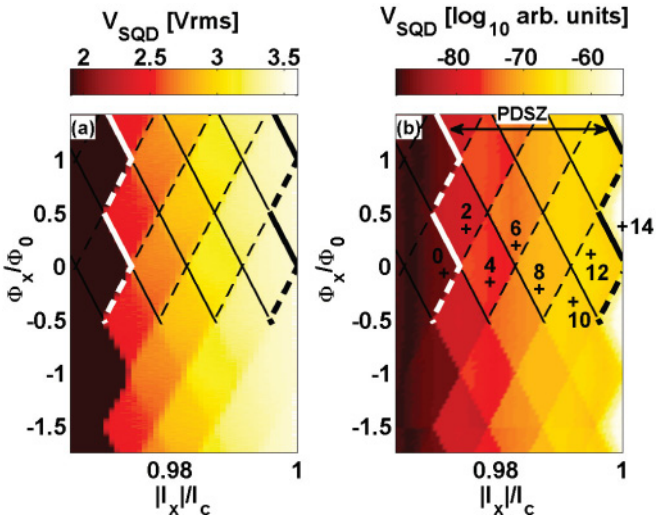

FIG. 5. (Color online) (a) Direct voltage measurements and (b) numerical calculations of the voltage across $E38$ dc SQUID in the plane of I_x and Φ_x. The stability diagram of $E38$ is plotted using black contours on both panels, where solid lines are used for $I_x > 0$ and dashed lines are used for $I_x < 0$. The diagram is applied only on half of the color maps in order to leave some data uncovered. The white bold contour marks the PDSZ threshold. Black bold contour marks the oscillatory threshold. Each plus sign marks a set of control parameters, and the corresponding number counts the LSZ boundaries that the SQUID periodically crosses if excited by that set of parameters.

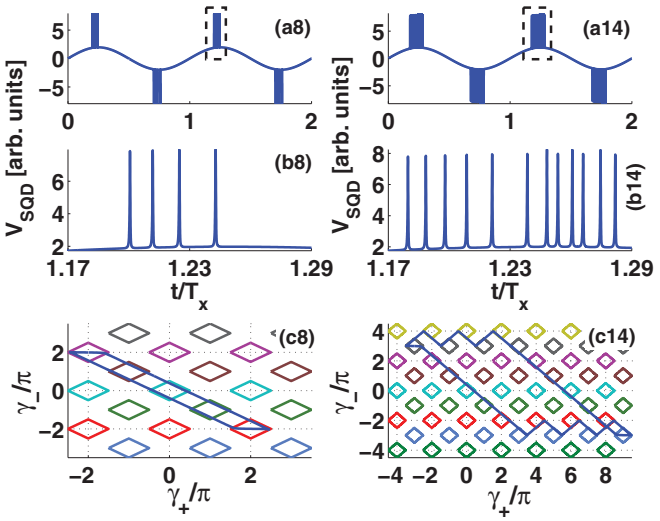

FIG. 6. (Color online) Simulation results for $E38$. Panels (ai), where $i = 8,14$ corresponding to the marked points in Fig. 5, plot the dc-SQUID voltage in the time domain. Panels (bi) magnify the corresponding marked squares in panels (ai). Panels (ci) show the simulation results and the corresponding stability zones in the phase space of γ_+ and γ_-.

positive or negative currents, triggers a spike, which in turn contributes additively to the measured voltage across the dc SQUID. Thus, each diamond bounds a range of parameters for which a similar voltage is measured. The diamonds follow the periodicity properties dictated for the control parameters by Eqs. (2) and (3).

We define an additional threshold, marked by the bold white contour in Fig. 5, that separates the static zone into two sections. In the first, which applies for periodic excitation currents smaller (in absolute value) than this threshold, the dc SQUID is captured in a single LSZ after a finite number of excitation cycles, and no spikes in the voltage appear afterwards. We call this section the periodic nondissipative static zone (PNDSZ). In the second section, which spreads for excitation currents larger than the white threshold but smaller than the oscillatory threshold, the SQUID periodically jumps between LSZs and dissipates energy. Thus, we call this section the periodic dissipative static zone (PDSZ), and call the white threshold itself the PDSZ threshold.

Figure 6 shows results of two simulations, which are calculated using the control parameters marked by points $i = [8,14]$ in Fig. 5. Panels (ai) show the dc-SQUID voltage as a function of time, calculated during two excitation cycles. Each cycle has a bunch of spikes during its positive duration and another bunch during the negative one. Panels (bi) magnify the corresponding bunch of spikes marked by dashed squares in panels (ai). In panel (b8), one counts four spikes corresponding to four crossings of stability thresholds. Panel (c8) shows the phase space dynamics in the plane of γ_- and γ_+. The system periodically cycles between five LSZs, where most of the time it lingers either in the upper left or in the lower right LSZs. The transition between these LSZs is forced by the driving sinusoidal bias current, which induces four jumps, corresponding to the four spikes in panel (b8). Panels (b14) and (c14) show a richer dynamics, which emerges from the fact that point $+14$ is located inside the oscillatory zone. The dynamics includes both forced transitions between LSZs and spontaneous oscillations related to the oscillatory zone. These two kinds of transitions are clearly seen in Fig. 6, panel (c14), which plots the dynamics of γ_+ and γ_- in the phase space. The first kind, in which γ_- and γ_+ change monotonically, corresponds to forced transitions between LSZs. The second kind, in which the system oscillates between LSZs, corresponds to the spontaneous oscillatory dynamics. The spontaneous oscillations last as long as the temporal driving bias current is greater than the oscillatory threshold. The distinction between the forced transitions and the spontaneous oscillations can also be noticed in the time domain, shown in Fig. 6, panel (b14), where the first six spikes are similar and distinct, whereas the rest of the spikes emerge in pairs, in which one spike is slightly stronger than the other.

B. Hybrid oscillatory zones

Figure 7 shows low-frequency experimental measurements of $E42$ dc SQUID, which has a self-inductance parameter of $\beta_L = 83$. Similar to the experiment with $E38$, we excite the SQUID with a sinusoidal current having frequency of $\omega_x/2\pi = 2.5$ kHz, and measure the voltage across the dc SQUID as a function of excitation current I_x and external magnetic flux Φ_x. In addition, we measure the spectral density of the voltage using a spectrum analyzer and its response in the time domain using an oscilloscope. Figure 7(a) shows this voltage and has the corresponding folded stability diagram drawn on it. The color map, which focuses on the oscillatory threshold, reveals an interesting phenomenon. The threshold related to positive excitation currents (solid bold line) is shifted compared to the one related to negative excitation currents (dashed bold line). This mismatch between the thresholds creates hybrid oscillatory zones, in which the dc SQUID is driven to the oscillatory zone either for positive currents or negative currents, but not for both.

Figure 7(b) plots a color map of the voltage noise level, measured using the spectrum analyzer at a frequency of 1 kHz (any frequency that is not an integer harmonics of ω_x gives similar results). Monitoring the noise level allows sensitive detection of thresholds since noise rise is generally expected near any bifurcation threshold.[52] Two distinct patterns of noise rise are clearly seen in the color map. One is related to the solid-line positive threshold and the other to the dashed-line negative threshold. Note that this noise rise is almost undetectable in the lock-in measurements.

The existence of hybrid zones is easily observed in time-domain measurements. Figure 8 shows two pairs of time-domain traces; each pair has an experimental trace [panels (1e) and (2e)] and a simulated trace [panels (1s) and (2s)], measured (calculated) for the parameters labeled by plus marks and the corresponding number in Figs. 7(a) and 7(b). The first (second) pair is related to the hybrid zone where only positive (negative) currents drive the system to the oscillatory zone. Accordingly, the first (second) pair experiences only positive (negative) spikes. The difference between the measured and simulated line shapes of the spikes might be due to finite (about one MHz) bandwidth of our measurement setup, which is far too low to resolve high-frequency spikes.

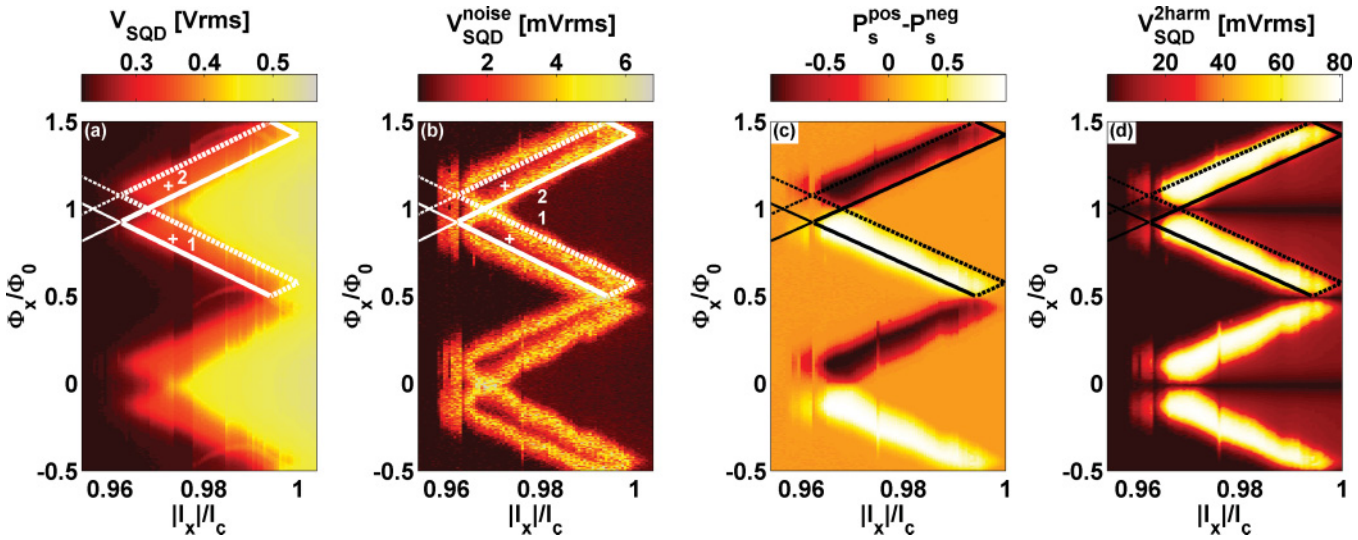

FIG. 7. (Color online) Experimental measurements obtained with $E42$. Panels (a) and (d) draw the first and second SQUID voltage harmonics, respectively. Panel (b) draws the voltage noise level at a frequency of 1 kHz. Panel (c) draws the difference between probabilities of measuring positive and negative voltage spikes, respectively. This statistical analysis is based on time-domain voltage traces.

Therefore, measured spikes in the output signal merge into one continuous and slowly decaying pulse. Local heating effects, which are neglected in this simulation and will be discussed later, may also degrade dc-SQUID performance and suppress the spikes.

A statistical analysis of the time-domain behavior is summarized in Fig. 7(c) for the parameter range spanned by I_x and Φ_x. The analysis calculates the probability of counting a positive spike $P_s^{\rm pos}$ minus the probability of counting a negative one $P_s^{\rm neg}$ during a single lock-in excitation cycle. Each data point is calculated using 2-s-long voltage time traces, obtained with current excitation frequency of $\omega_x/2\pi = 2.5$ kHz. The resulting color map clearly reveals the existence of the hybrid oscillatory zones, where the differential probability of counting spikes having either positive or negative polarities is almost one. The direction of the spikes agrees with the prediction of the stability diagram. Outside the hybrid zones, the color map shows near zero differential probability. In these areas, there are no spikes at all, or the counting of positive and negative spikes is similar. This behavior could be used for creating bidirectional dc-SQUID sensors in which the polarity of measured voltage indicates the polarity of the detected flux change. Panel (d) plots the second harmonics of the measured SQUID voltage (at 5 kHz). This harmonics is expected to be amplified when the measured voltage is asymmetric in time, i.e., neither symmetric nor antisymmetric time response. The hybrid zones are characterized by such a time response, and indeed, the plotted color map shows strong response of the second harmonics in those zones.

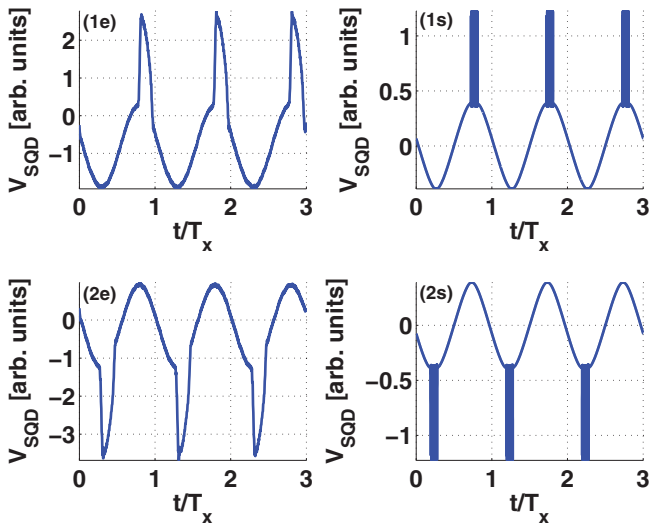

FIG. 8. (Color online) Time-domain experimental measurements (left column) and numerical simulations (right column) of $E42$. The two rows correspond to the two sets of control parameters marked in Fig. 7.

V. HIGH-FREQUENCY TLR-SQUID DYNAMICS

In recent years, several demonstrations of using SQUIDs to manipulate the resonance frequencies of a superconducting resonator were reported.[15–17,34] A SQUID in such applications is usually considered as a nonlinear variable inductor embedded in the resonator in a way that couples the resonance frequencies of the resonator to the SQUID impedance. The variation of the SQUID inductance is usually done by changing the magnetic flux through the SQUID, whereas the current through the SQUID is defined by power of the tone exciting the resonator and by the state of the coupled system.

A. Stability zones

In the following, we analyze the stability of a dc SQUID, excited by a magnetic flux having constant and alternating parts. Consider the case where Φ_x is given by

$$\Phi_x = \Phi_x^{\rm dc} + \Phi_x^{\rm ac}\cos(\omega_{px}t), \tag{10}$$

where $\Phi_x^{\rm dc}/\Phi_0$ and $\Phi_x^{\rm ac}/\Phi_0$ are arbitrary amplitudes. Recall that, for the case of $\beta_L \gg 1$, and for the minimum point

near $(\gamma_+,\gamma_-)=(0,0)$, the bounding rectangle crosses the axis $I_x=0$ at the points $\Phi_x=\pm\Phi_0\widetilde{\beta}_L/2\pi$, where $\widetilde{\beta}_L=(1-\alpha)\beta_L$. The range of stability for the minima points near $(\gamma_+,\gamma_-)=(n\pi,n\pi)$, where n is integer, is given by

$$-\frac{\widetilde{\beta}_L}{2\pi}+n\leqslant\frac{\Phi_x}{\Phi_0}\leqslant\frac{\widetilde{\beta}_L}{2\pi}+n. \tag{11}$$

Furthermore, the stability condition is achieved when the largest value of Φ_x, i.e., $\Phi_x^{\rm dc}+\Phi_x^{\rm ac}$, coincides with the largest value of the stability range, i.e. $\widetilde{\beta}_L/2\pi$, or when the smallest value of Φ_x, i.e., $\Phi_x^{\rm dc}-\Phi_x^{\rm ac}$, coincides with the smallest value of the stability range, i.e., $-\widetilde{\beta}_L/2\pi$. Thus, the boundary contours in the plan of $\Phi_x^{\rm dc}$ and $\Phi_x^{\rm ac}$ are given by the two equations

$$\Phi_x^{\rm dc}\pm\Phi_x^{\rm ac}=\pm\Phi_0\frac{\widetilde{\beta}_L}{2\pi}+n\Phi_0. \tag{12}$$

B. Parametric excitation

In experiments with resonators, we employ the parametric excitation method of operation.[18–21] We inject a relatively weak probing signal into the resonator, having frequency equal to one of the resonance frequencies of the resonator ω_x, and measure the reflected power off the resonator using a spectrum analyzer. Note that the dc connections do not play any role in this measurement. A weak signal is one for which the current generated through the SQUID is much smaller than its critical current. In addition, we applied constant and variable magnetic flux through the SQUID, given by Eq. (10) with $\omega_{px}=(2\omega_x+\Delta\omega)$, where $\Delta\omega$ is taken to be much smaller than the resonance bandwidth of the resonator. The measured reflected power spectrum includes a tone at ω_x and several sidebands spaced by $\pm m\cdot\Delta\omega$ from ω_x, where m is an integer. These sidebands are the products of the nonlinear frequency mixing between ω_x and ω_{px}. Although this mixing process is more complex than our direct SQUID measurements, it should essentially follow the same SQUID dynamics, provided that adiabatic approximation is not violated, namely, $\omega_x\ll\omega_{\rm pl}$. Therefore, we expect the various tones to reflect that dynamics.

Figure 9(a) shows the folded stability diagram, drawn in the plane of $\Phi_x^{\rm dc}$ and $\Phi_x^{\rm ac}$ using Eq. (12) and $\widetilde{\beta}_L=45$. The solid and dashed lines represent stability thresholds for positive and negative polarities of $\Phi_x^{\rm ac}$, respectively. Four pairs of solid-dashed lines are drawn, with each corresponding to a different number of flux quanta trapped in the SQUID. The black bold line marks the threshold between the PNDSZ and the PDSZ. Namely, for excitation amplitudes $|\Phi_x^{\rm ac}|$ smaller than the black line, the SQUID will reach a LSZ after a finite number of excitation periods. On the other hand, for $|\Phi_x^{\rm ac}|$ higher than the black line, the SQUID will periodically jump between LSZs. Note that in this method of excitation, where the injected current is kept much smaller than the critical current, the SQUID would not be driven to the oscillatory zone, even by an arbitrarily large $\Phi_x^{\rm ac}$.

Figure 10(b) shows the simulated second voltage harmonics across the SQUID, i.e., at frequency $\omega=2\omega_{px}$, and for $\Delta\omega=0$, obtained using $E42$ parameters. The black contours, which are similar to the ones in Fig. 9(a), mark the stability diagram. The distinction between the periodic nondissipative

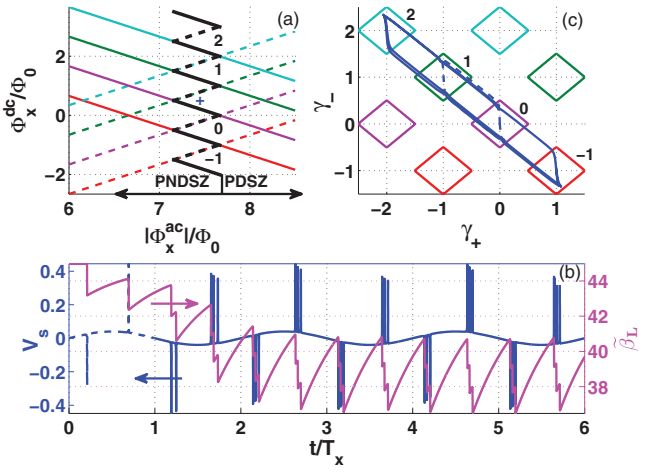

FIG. 9. (Color online) (a) Stability zones in the plan of the control parameters $\Phi_x^{\rm ac}$ and $\Phi_x^{\rm dc}$, drawn for $\widetilde{\beta}_L=45$. The curves are drawn using solid lines for $\Phi_x^{\rm ac}>0$ and dashed lines for $\Phi_x^{\rm ac}<0$. The numbers beside each pair crossing represent the total magnetic flux quanta trapped in the SQUID in the corresponding LSZ (in units of Φ_0). The bold black curve marks the PDSZ threshold. Simulation results of the SQUID voltage and $\widetilde{\beta}_L$ in the normalized time domain (b), and γ_+ and γ_- in the phase space (c). The simulation is calculated using the set of control parameters marked by the plus sign in panel (a). Time is normalized by T_x, which is the period of probing tone injected to the resonator.

and periodic dissipative static zones is clear, and is marked by the white bold PDSZ threshold. As before with the dc SQUID of $E38$, the PDSZ is characterized by relatively high SQUID voltage, which is divided into diamond-shaped regions. The PNDSZ, unlike what was found with $E38$, is also characterized by strong response along the stability contours. Crossing of one such contour triggers a single transition between LSZ, which is not followed by additional periodic transitions between LSZ. Nevertheless, these boundaries are detectable due to the fact that the inductance of the SQUID before and after a transition is different, and also due to the fact that the excitation frequency is high, thus the effect of changes in the SQUID inductance is measurable. Only transitions across the solid stability contours are observed in the color map of Fig. 10. The reason for this is related to the measurement protocol, which includes sweeping the dc flux monotonically up and down in the inner simulation loop. The color map is obtained while the flux amplitude is increased, thus transitions over the solid contours are recorded, whereas the decreasing section is only used to maintain the consecutiveness of initial condition, similar to the experiments.

Figure 10(a) shows measurement results obtained from $E42$. A probe tone having frequency of ω_x is injected into the resonator, and the reflected power of the second-order sideband, i.e., the tone at $\omega_x+\Delta\omega$, is measured, while the dc flux is swept up (blue curve, marked by up-headed arrow) and down (red curve, marked by down-headed arrow), and while keeping the ac flux at a fixed amplitude. Following the blue curve from bottom to top, the reflected power experiences a resonance-like absorption followed by a saw-teeth pattern. The resonance absorption pattern originates from the tuning of the resonance frequency of the resonator relatively to the frequency of the probing signal, thus effectively sweeping

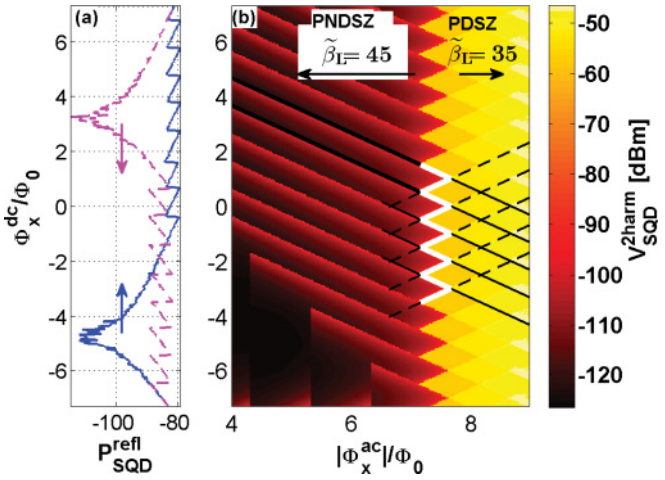

FIG. 10. (Color online) Parametric excitation experimental (a) and simulation (b) results. (a) Reflected power of the second voltage harmonics as a function of increasing (dark blue) and decreasing (light magenta) dc flux. (b) Simulated second voltage harmonics in the plane of Φ_x^{ac} and Φ_x^{dc}. The black contours mark the corresponding stability diagram drawn for $\widetilde{\beta}_L = 45$. White bold contours mark the threshold to the PDSZ.

the probe in and out of resonance. This sweeping is caused by the SQUID, which has flux-dependent inductance,[34] even when stuck in a single LSZ. After the SQUID is driven across a stability threshold, it falls to a new LSZ, into a location that is one flux quantum away from the corresponding stability contour. Thus, if the external flux is further increased, it would further drive the SQUID to the same direction, and additional transitions would occur, spaced apart by one flux quantum. If, on the other hand, the direction of the sweep changes (red curve), the SQUID would first have to be driven across a whole LSZ until reaching the opposite stability threshold. Therefore, no matter where the flux sweep changes direction along the saw-teeth pattern, the reflected power would experience a resonancelike absorption followed by saw-teeth pattern.

Looking back at Fig. 10(b), the sweeping of Φ_x^{dc} up and down usually drives back the SQUID to its original LSZ. When the ac flux amplitude Φ_x^{ac} is increased, the borders of a LSZ converge one to the other. As a result, the sweep across the first stability zone becomes shorter, and hence the resonance absorption pattern becomes narrower along the dc flux axis. This narrowing adds additional saw teeth along the sweep range, and in addition, the SQUID might no longer return to its original LSZ, but rather to a new LSZ, which corresponds to a change of one in the number of trapped flux quanta. This creates the sharp transition observed in the resonancelike absorption patterns along the horizontal axis.

C. Temperature-dependent critical current

When a SQUID is embedded in a resonator, the current I_x flowing through the SQUID is driven by the resonator, and thus its frequency equals to one of the resonance frequencies of the resonator. These first few frequencies are only about two to three orders of magnitude lower than the plasma frequency of the SQUID.[34] Furthermore, the heat-transfer rate corresponding to hot spots in the NBJJs may be on the order of those frequencies or even slower.[40] Therefore, the effect of local heating of the NBJJs on the dynamics of the SQUID must be taken into account. Assume, for simplicity, that the temperature T_k ($k = 1,2$) in each NBJJ is uniform. The dependence of the critical current on the temperature is given by[53]

$$\frac{I_{ck}}{I_{c0k}} = y(\Theta_k) \equiv \frac{\widetilde{y}(\Theta_k)}{\widetilde{y}(\Theta_0)}, \tag{13}$$

where I_{c0k} is the critical current of kth NBJJ at base temperature T_0 of the coolant, $\Theta_k = T_k/T_c$ is normalized temperature of the NBJJ (with respect to its critical temperature), $\Theta_0 = T_0/T_c$, and where the function $\widetilde{y}$ is given by

$$\widetilde{y}(\Theta) = (1-\Theta^2)^{3/2}(1+\Theta^2)^{1/2}. \tag{14}$$

The two NBJJ heat balance equations read as

$$C_k \frac{dT_k}{dt} = Q_k - H_k(T_k - T_0), \tag{15}$$

where $k = 1,2$ is the junction number, C_k is thermal heat capacity, $Q_k = V_k^2/R_J$ is heating power, and H_k is the heat-transfer coefficient. By using the notation $\beta_{Ck} = 2\pi C_k T_c/\Phi_0 I_{c0}$ and $\beta_{Hk} = H_k C_k \omega_p$, Eq. (15) becomes

$$\dot{\Theta}_k = \frac{\beta_D}{\beta_{Ck}}\dot{\gamma}_k^2 - \beta_{Hk}(\Theta_k - \Theta_0). \tag{16}$$

Figure 9, panels (b) and (c), show simulation results of the SQUID voltage and $\widetilde{\beta}_L$ in the time domain (b), and the SQUID phases (c), calculated for the control parameters marked by the plus sign in Fig. 9(a). In this simulation, the temperatures of the NBJJs are not held at the base temperature, but rather evolve according to Eq. (16). The parameters $\beta_{Ck} = 320$ and $\beta_{Hk} = 5 \times 10^{-4}$ ($k = 1,2$) were calculated analytically according to Refs. 54–56. Further explanations about calculation of parameters are found in Appendix B of Ref. 34. One expects that, for the chosen control parameters, the SQUID would oscillate between two LSZs. However, the dynamic behavior of the SQUID, plotted in panel (c), indicates that this is true only during the first excitation cycle (dashed line) and that afterwards the SQUID oscillates between four LSZs. Corresponding dynamical change in the behavior of the SQUID voltage response can be observed in the time trace plotted in panel (b). The total number of voltage spikes in each excitation cycle increases from two, during the first excitation cycle (dashed line), to six during the third excitation cycle (solid line). This behavior can be explained by the dynamical change in the value of $\widetilde{\beta}_L$, plotted by a red curve in panel (b). The screening parameter $\widetilde{\beta}_L$ experiences relaxation oscillations having their mean value changing during the first three excitation cycles. The relaxation oscillations are driven by the voltage spikes, which dissipate energy and produce heat. This heat increases the temperature of the NBJJs, which, in turn, decreases their critical current according to Eq. (13), thus decreasing the value of β_L. The reduction in β_L results in a shift of the stability diagram toward the origin, and consequently the given set of control parameters effectively drives the SQUID between increased numbers of LSZs.

Figure 11 shows the reflected power of the second-order mixing product, i.e., the tone at $\omega_x + \Delta\omega$, measured in the plane of Φ_x^{dc} and Φ_x^{ac} from $E42$. This measurement

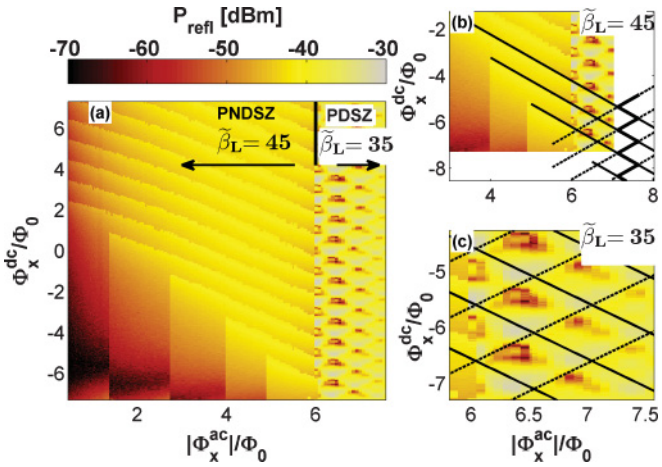

FIG. 11. (Color online) Parametric excitation experimental results. The color maps show the reflected power off the resonator in the plane of Φ_x^{ac} and Φ_x^{dc}. Panels (b) and (c) show the fitting of the stability diagram to the measured data using $\widetilde{\beta}_L = 45$ and 35, respectively. Note that the stability diagram in panel (b) covers an area bigger than the area for which experimental data were obtained.

corresponds to the simulation shown in Fig. 10. The figure contains three panels, where panels (b) and (c) show partial sections of the main color map shown in panel (a), each with a corresponding fit of the stability diagram. Looking at panel (a), most of the observations qualitatively agree with the simulated results seen in Fig. 10. The PDSZ is characterized by strong reflection response and by stability regions having diamond shapes. The PNDSZ experiences strong response along the boundaries of the LSZs. The response lines slightly bend for low excitation amplitudes ($\Phi_x^{ac} \lesssim 3\Phi_0$), but follow rather straight lines for higher amplitudes. The best fitting of the stability diagram to these lines is achieved with $\widetilde{\beta}_L = 45$, as shown in panel (b). The slight bending of the boundary lines that occur as the ac excitation amplitude increases may be due to a rise of the average temperatures of the SQUID. The reason why only transitions across solid stability contours are measured is the measurement protocol, which includes a sweep of the dc flux up and down in the inner measurement loop, while measurements are recorded only during the incremental part of the sweep. In addition to the emerging of the LSZ boundaries in the measurement, also the influence of the variation of the SQUID inductance within a LSZ on the reflected power is observed. Furthermore, the sharp transitions along the horizontal axis, corresponding to dc flux sweeps that do not drive the SQUID back to its original LSZ, are observed at $\Phi_x^{ac}/\Phi_0 = [1.4, 2.75, 4.05, 4.74]$, in agreement with the simulation results.

The fitting process of the stability diagram to the experimental data shown in Fig. 11 reveals a discrepancy in the value of the fitting parameter $\widetilde{\beta}_L$. The stability diagram in Fig. 11(b), drawn for $\widetilde{\beta}_L = 45$, predicts that the PDSZ threshold should zigzag along the stability contours in the range of $\Phi_x^{ac}/\Phi_0 \in [7.5, 8]$. The measured color map, however, shows that the PDSZ threshold passes along a straight vertical line starting at point $(\Phi_x^{dc} = -6.25\Phi_0, \Phi_x^{ac} = 5.95\Phi_0)$. In addition, although the predicted threshold contour falls beyond the scope of the experimental data presented in Fig. 11(b), other measurements, which include this area but are not presented here, show no unusual threshold dynamics in that range. Furthermore, the stability diagram in Fig. 11(c), which best matches to the diamond shapes of the PDSZ section, is drawn using $\widetilde{\beta}_L = 35$.

This duality in the value of $\widetilde{\beta}_L$ can be understood if changes in the SQUID temperature are taken into account. The PDSZ threshold point exactly coincides with one of the LSZ threshold contours. The heat generated in a single transition across that threshold momentarily decreases $\widetilde{\beta}_L$. An additional transition may be triggered provided that the relaxation of the first one lasts long enough, which, in turn, may cause further heating of the dc SQUID. Eventually, a new mean temperature is achieved for which $\widetilde{\beta}_L = 35$. The measurement protocol dictates that this new temperature would be kept and that the dc SQUID would stay in the PDSZ for the rest of the measurement. Note that the initial value of $\widetilde{\beta}_L = 45$ differs from the value of $\widetilde{\beta}_L = 80$ that was measured using the lock-in amplifier. This can be explained by the local heating that the high-frequency flux excitation induces in the dc SQUID, especially in the NBJJs, through the dissipation of circulating current due to rf surface resistance. Such a reduction in $\widetilde{\beta}_L$, from 80 to 45, corresponds to a change of the local temperature by approximately 2 K.

D. Case of rf SQUID parametric excitation

The stability diagram for a dc SQUID can be evaluated numerically or be analytically approximated for the extreme cases of $\beta_L \ll 1$ and $\beta_L \gg 1$. For the rf SQUID, on the other hand, it could be exactly evaluated analytically. Consider a rf SQUID having self-inductance L, critical current I_c, and externally applied magnetic flux $\Phi_x = (\Phi_0/2\pi)\phi_x$. The dynamics of the total magnetic flux $\Phi = (\Phi_0/2\pi)\phi$ threading the rf SQUID loop is governed by the potential energy $U = U_0 u_{\rm rf}$,[57] where

$$u_{\rm rf} = (\phi - \phi_x)^2 - 2\beta_L \cos\phi, \tag{17}$$

and $U_0 = \Phi_0^2/(8\pi^2 L)$. A local minimum point of $u_{\rm rf}$ is found by solving $\partial u_{\rm rf}/\partial\phi = 0$ and requiring that $\partial^2 u/\partial\phi^2 > 0$. Clearly, if ϕ_m is a local minimum point of the potential $u_{\rm rf}$ with a given ϕ_x, then $\phi_m + 2n\pi$ is also a local minimum point of the potential $u_{\rm rf}$ with an externally applied flux of $\phi_x + 2n\pi$, provided that n is integer.

Loss of stability occurs when $\partial^2 u/\partial\phi^2 = 0$, namely, when $\cos\phi = -1/\beta_L$. This can occur only when $\beta_L > 1$, since otherwise the system is expected to be monostable. This condition is satisfied when $\phi_x = \phi_{x,b}$, where

$$\phi_{x,b} = \pi - \arccos\left(\frac{1}{\beta_L}\right) + \sqrt{\beta_L^2 - 1}. \tag{18}$$

For a general integer n, the local minimum of the potential $u_{\rm rf}$ near $\phi = 2n\pi$ remains stable in the range

$$-\phi_{x,b} + 2n\pi \leqslant \phi_x \leqslant \phi_{x,b} + 2n\pi. \tag{19}$$

Similar to the case of the dc SQUID, where Φ_x is given by Eq. (10), the boundary contours in the plan of Φ_x^{dc} and Φ_x^{ac} are given by the two equations

$$\Phi_x^{dc} \pm \Phi_x^{ac} = \Phi_0\left(\pm\frac{\phi_{x,b}}{2\pi} + n\right), \tag{20}$$

for the largest and smallest values of Φ_x, respectively.

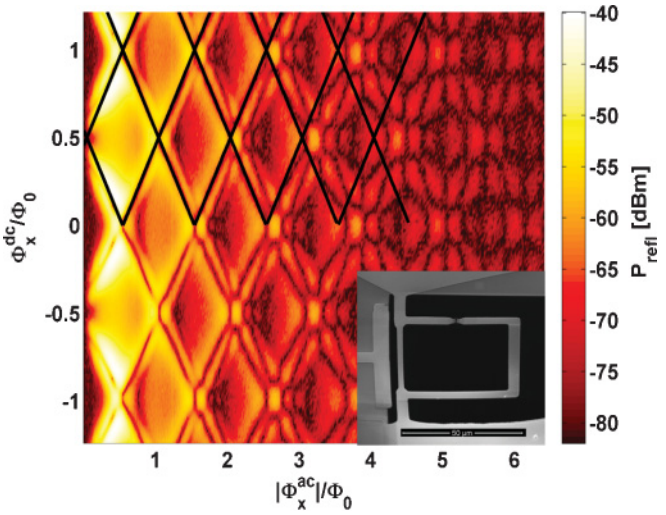

FIG. 12. (Color online) Parametric excitation experimental results using $E19$, which has an integrated rf SQUID. The color map shows the reflected power off the resonator in the plane of Φ_x^{ac} and Φ_x^{dc}. The black contours mark the corresponding stability diagram. They are applied only on half of the color map in order to leave some data uncovered. The inset shows an electron micrograph of a rf SQUID.

Figure 12 shows the reflected power of the third-order mixing product, i.e., the tone at $\omega_x + 2\Delta\omega$, measured in the plane of Φ_x^{dc} and Φ_x^{ac} with $E19$, which has an embedded rf SQUID instead of a dc SQUID. The black contours represent the stability diagram, plotted using Eq. (20) for $\beta_L = 1.5$. The stability diagram qualitatively matches the measured data for the first few stability diamonds.

Note that the value of β_L for the rf SQUID of $E19$ is more than an order of magnitude smaller than that of $E38$ and $E42$. This might be due to the fact that this rf SQUID is fully fabricated on a silicon nitride membrane, and thus has reduced thermal coupling to the coolant compared to the dc SQUIDs of $E38$ and $E42$. This in turn might lead to an increased local temperature of the NBJJ, and to a degraded value of β_L.[41]

Note also that the diamonds themselves have distinct patterns inside their bounded zone (see Figs. 11 and 12), which are not perfectly periodic with Φ_x^{ac}, but are reproducible in measurements. They are only detected in measurements with resonators having either dc or rf SQUIDs, but not in measurements done directly with dc SQUIDs. Our model only handles the dc SQUID equations of motion, and thus can not provide full description of the dynamics of the resonator-SQUID system. Further theoretical work is needed for modeling combined TLR-SQUID systems in order to fully understand these experimental results.

VI. CONCLUSIONS

In conclusion, we have studied the response of a nanobridge-based SQUID embedded in a superconducting microwave resonator. Nanobridge-based SQUIDs are usually characterized by high critical current, and thus enhanced metastable and hysteretic response. Several phenomena were observed, including the periodic dissipative static zone in which periodic transitions between local stable states occur, hybrid oscillatory zones, in which the SQUID is driven to the oscillatory zone by one polarity of the excitation amplitude but not for the other, and dynamical variations in β_L due to the effect of self-heating. The behaviors of the SQUIDs were compared with theory both analytically and numerically with good agreement.

ACKNOWLEDGMENTS

This work was supported by the Adams Program of the Israel Academy of Sciences and Humanities, the German Israel Foundation under Grant No. 1-2038.1114.07, the Israel Science Foundation under Grant No. 1380021, the Deborah Foundation, the Poznanski Foundation, Russell Berrie Nanotechnology Institute, Israeli Ministry of Science, the European STREP QNEMS project, and MAFAT.

APPENDIX: NANOBRIDGE CURRENT-PHASE RELATION

The CPR of a single short channel of transmission τ is given by[50]

$$I = \frac{e\Delta}{2\hbar} J(\gamma), \tag{A1}$$

where

$$J(\gamma) = \frac{\tau \sin\gamma}{\sqrt{1 - \tau \sin^2 \frac{\gamma}{2}}}. \tag{A2}$$

The NBJJs in our devices are not ideal one-dimensional point contacts as Ref. 50 assumes; however, we have found that the above simple analytical result resembles the CPR that is obtained by solving the Ginzburg-Landau equation in the limit of short bridge (in comparison with the coherence length).[24] Let γ_0 be the point at which the factor $J(\gamma)$ has its largest value $J(\gamma_0)$, which is given by

$$J(\gamma_0) = 2\sqrt{2(1 - \sqrt{1-\tau}) - \tau}. \tag{A3}$$

By using this result, the current I can be written in terms of I_c as $I/I_c = F(\gamma)$, where

$$F(\gamma) = \frac{\tau \sin\gamma}{2\sqrt{2(1 - \sqrt{1-\tau}) - \tau}\sqrt{1 - \tau \sin^2 \frac{\gamma}{2}}}. \tag{A4}$$

Replacing the $\sin\gamma_k$ terms ($k = 1,2$) in Eqs. (7) and (8) by $F(\gamma_k)$ leads to the following modified EOMs:

$$\ddot{\gamma}_1 + \beta_D \dot{\gamma}_1 + (1+\alpha_0) y(\Theta_1) F(\gamma_1) + \frac{1}{\beta_{L0}}(\gamma_1 - \gamma_2 + 2\pi\Phi_x/\Phi_0) = I_x/I_{c0} + g_{n1} \tag{A5}$$

and

$$\ddot{\gamma}_2 + \beta_D \dot{\gamma}_2 + (1-\alpha_0) y(\Theta_2) F(\gamma_2) - \frac{1}{\beta_{L0}}(\gamma_1 - \gamma_2 + 2\pi\Phi_x/\Phi_0) = I/I_{c0} + g_{n2}. \tag{A6}$$

*segeve@tx.technion.ac.il
†Current address: University of Basel, Basel, Switzerland.

[1] I. Chiorescu, P. Bertet, K. Semba, Y. Nakamura, C. J. P. M. Harmans, and J. E. Mooij, Nature (London) **431**, 159 (2004).
[2] J. Johansson, S. Saito, T. Meno, H. Nakano, M. Ueda, K. Semba, and H. Takayanagi, Phys. Rev. Lett. **96**, 127006 (2006).
[3] A. A. Houck, D. I. Schuster, J. M. Gambetta, J. A. Schreier, B. R. Johnson, J. M. Chow, L. Frunzio, J. Majer, M. H. Devoret, S. M. Girvin *et al*., Nature (London) **449**, 328 (2007).
[4] J. Majer, J. M. Chow, J. M. Gambetta, J. Koch, B. R. Johnson, J. A. Schreier, L. Frunzio, D. I. Schuster, A. A. Houck, A. Wallraff, A. Blais, M. H. Devoret, S. M. Girvin, and R. J. Schoelkopf, Nature (London) **449**, 443 (2007).
[5] M. A. Sillanpaa, J. I. Park, and R. W. Simmonds, Nature (London) **449**, 438 (2007).
[6] O. Astafiev, A. M. Zagoskin, A. A. Abdumalikov Jr., Y. A. Pashkin, T. Yamamoto, K. Inomata, Y. Nakamura, and J. S. Tsai, Science **327**, 840 (2010).
[7] A. Lupascu, E. F. C. Driessen, L. Roschier, C. J. P. M. Harmans, and J. E. Mooij, Phys. Rev. Lett. **96**, 127003 (2006).
[8] J. C. Lee, W. D. Oliver, K. K. Berggren, and T. P. Orlando, Phys. Rev. B **75**, 144505 (2007).
[9] A. Lupascu, C. J. M. Verwijs, R. N. Schouten, C. J. P. M. Harmans, and J. E. Mooij, Phys. Rev. Lett. **93**, 177006 (2004).
[10] R. J. Schoelkopf and S. M. Girvin, Nature (London) **451**, 664 (2008).
[11] F. Mallet, F. R. Ong, A. Palacios-Laloy, F. Nguyen, P. Bertet, D. Vion, and D. Esteve, Nat. Phys. **5**, 791 (2009).
[12] N. Bergeal, F. Schackert, M. Metcalfe, R. Vijay, V. E. Manucharyan, L. Frunzio, D. E. Prober, R. J. Schoelkopf, S. M. Girvin, and M. H. Devoret, Nature (London) **465**, 64 (2010).
[13] R. Vijay, M. H. Devoret, and I. Siddiqi, Rev. Sci. Instrum. **80**, 111101 (2009).
[14] O. V. Astafiev, A. A. Abdumalikov, A. M. Zagoskin, Y. A. Pashkin, Y. Nakamura, and J. S. Tsai, Phys. Rev. Lett. **104**, 183603 (2010).
[15] M. Sandberg, C. M. Wilson, F. Persson, T. Bauch, G. Johansson, V. Shumeiko, T. Duty, and P. Delsing, Appl. Phys. Lett. **92**, 203501 (2008).
[16] M. A. Castellanos-Beltran and K. W. Lehnert, Appl. Phys. Lett. **91**, 083509 (2007).
[17] A. Palacios-Laloy, F. Nguyen, F. Mallet, P. Bertet, D. Vion, and D. Esteve, J. Low Temp. Phys. **151**, 1034 (2008).
[18] M. A. Castellanos-Beltran, K. D. Irwin, G. C. Hilton, L. R. Vale, and K. W. Lehnert, Nat. Phys. **4**, 929 (2008).
[19] M. A. Castellanos-Beltran, K. D. Irwin, L. R. Vale, G. C. Hilton, and K. W. Lehnert, IEEE Trans. Appl. Supercond. **19**, 944 (2009).
[20] E. A. Tholén, A. Ergl, K. Stannigel, C. Hutter, and D. B. Haviland, Phys. Scr. **2009**, 014019 (2009).
[21] T. Yamamoto, K. Inomata, M. Watanabe, K. Matsuba, T. Miyazaki, W. D. Oliver, Y. Nakamura, and J. S. Tsai, Appl. Phys. Lett. **93**, 042510 (2008).
[22] J. R. Johansson, G. Johansson, C. M. Wilson, and F. Nori, Phys. Rev. Lett. **103**, 147003 (2009).
[23] C. Wilson, T. Duty, M. Sandberg, F. Persson, V. Persson, and P. Delsing, e-print arXiv:1006.2540.
[24] K. K. Likharev, Rev. Mod. Phys. **51**, 101 (1979).
[25] A. G. P. Troeman, S. H. W. van der Ploeg, E. Il'Ichev, H.-G. Meyer, A. A. Golubov, M. Yu Kupriyanov, and H. Hilgenkamp, Phys. Rev. B **77**, 024509 (2008).
[26] K. Hasselbach, D. Mailly, and J. R. Kirtley, J. Appl. Phys. **91**, 4432 (2002).
[27] A. Troeman, H. Derking, B. Borger, J. Pleikies, D. Veldhuis, and H. Hilgenkamp, Nano Lett. **7**, 2152 (2007).
[28] L. Hao, D. C. Cox, and J. C. Gallop, Supercond. Sci. Technol. **22**, 064011 (2009).
[29] C. D. Tesche and J. Clarke, J. Low Temp. Phys. **29**, 301 (1977).
[30] A. A. J. Matsinger, R. de Bruyn Ouboter, and H. van Beelen, Physica B+C (Amsterdam) **94**, 91 (1978).
[31] V. Lefevre-Seguin, E. Turlot, C. Urbina, D. Esteve, and M. H. Devoret, Phys. Rev. B **46**, 5507 (1992).
[32] A. M. Goldman, P. J. Kreisman, and D. J. Scalapino, Phys. Rev. Lett. **15**, 495 (1965).
[33] T. A. Palomaki, S. K. Dutta, H. Paik, H. Xu, J. Matthews, R. M. Lewis, R. C. Ramos, K. Mitra, P. R. Johnson, F. W. Strauch *et al*., Phys. Rev. B **73**, 014520 (2006).
[34] O. Suchoi, B. Abdo, E. Segev, O. Shtempluck, M. P. Blencowe, and E. Buks, Phys. Rev. B **81**, 174525 (2010).
[35] L. Hao, J. C. Macfarlane, J. C. Gallop, D. Cox, P. Joseph-Franks, D. Hutson, J. Chen, and S. K. H. Lam, IEEE Trans. Instrum. Meas. **56**, 392 (2007).
[36] A. Datesman, J. Schultz, T. Cecil, C. Lyons, and A. Lichtenberger, IEEE Trans. Appl. Supercond. **15**, 3524 (2005).
[37] G. C. Tettamanzi, C. I. Pakes, A. Potenza, S. Rubanov, C. H. Marrows, and S. Prawer, Nanotechnology **20**, 465302 (2009), e-print arXiv:1003.5430.
[38] E. Segev, O. Suchoi, O. Shtempluck, and E. Buks, Appl. Phys. Lett. **95**, 152509 (2009).
[39] Fast field solvers [http://www.fastfieldsolvers.com/].
[40] M. Tarkhov, J. Claudon, J. P. Poizat, A. Korneev, A. Divochiy, O. Minaeva, V. Seleznev, N. Kaurova, B. Voronov, A. V. Semenov *et al*., Appl. Phys. Lett. **92**, 241112 (2008).
[41] E. Segev, O. Suchoi, O. Shtempluck, F. Xue, and E. Buks, e-print arXiv:1010.4391.
[42] W. Zahn, Phys. Status Solidi A **66**, 649 (1981).
[43] W.-T. Tsang and T. V. Duzer, J. Appl. Phys. **46**, 4573 (1975).
[44] A. Palacios, J. Aven, P. Longhini, V. In, and A. R. Bulsara, Phys. Rev. E **74**, 021122 (2006).
[45] E. Ben-Jacob, D. J. Bergman, Y. Imry, B. J. Matkowsky, and Z. Schuss, J. Appl. Phys. **54**, 6533 (1983).
[46] M. E. Inchiosa, A. R. Bulsara, K. A. Wiesenfeld, and L. Gammaitoni, Phys. Lett. A **252**, 20 (1999).
[47] K. Wiesenfeld, A. R. Bulsara, and M. E. Inchiosa, Phys. Rev. B **62**, R9232 (2000).
[48] J. F. Ralph, T. D. Clark, R. J. Prance, H. Prance, and J. Diggins, J. Phys. Condens. Matter **8**, 10753 (1996).
[49] J. Clarke and A. I. Braginski, *The SQUID Handbook: Fundamentals and Technology of SQUIDs and SQUID Systems*, 1st ed. (Wiley, New York, 2004).
[50] C. W. J. Beenakker and H. Van Houten, Phys. Rev. Lett. **66**, 3056 (1991).
[51] A. A. Golubov, M. Y. Kupriyanov, and E. Il'ichev, Rev. Mod. Phys. **76**, 411 (2004).
[52] B. A. Huberman, J. P. Crutchfield, and N. H. Packard, Appl. Phys. Lett. **37**, 750 (1980).

[53]W. J. Skocpol, Phys. Rev. B **14**, 1045 (1976).
[54]M. W. Johnson, A. M. Herr, and A. M. Kadin, J. Appl. Phys. **79**, 7069 (1996).
[55]K. Weiser, U. Strom, S. A. Wolf, and D. U. Gubser, J. Appl. Phys. **52**, 4888 (1981).
[56]R. Monticone, V. Lacquaniti, R. Steni, M. Rajteri, M. Rastello, L. Parlato, and G. Ammendola, IEEE Trans. Appl. Supercond. **9**, 3866 (1999).
[57]E. Buks and M. P. Blencowe, Phys. Rev. B **74**, 174504 (2006).